Combination Therapies to Improve the Efficacy of Immunotherapy in Triple-negative Breast Cancer

Maša Alečković[1,2,3], Zheqi Li[1,2,3], Ningxuan Zhou[1,4], Xintao Qiu[1,4], Bethlehem Lulseged[1,5], Pierre Foidart[1,2,3], Xiao-Yun Huang[1], Kodie Garza[1], Shaokun Shu[1,2,3], Nikolas Kesten[1,4], Rong Li[1,4], Klothilda Lim[1,4], Ana C. Garrido-Castro[1,2,3], Jennifer L. Guerriero[1,6], Jun Qi[1,2,3], Henry W. Long[1,4], and Kornelia Polyak[1,2,3]

ABSTRACT

Immune checkpoint inhibition combined with chemotherapy is currently approved as first-line treatment for patients with advanced PD-L1–positive triple-negative breast cancer (TNBC). However, a significant proportion of metastatic TNBC is PD-L1–negative and, in this population, chemotherapy alone largely remains the standard-of-care and novel therapeutic strategies are needed to improve clinical outcomes. Here, we describe a triple combination of anti-PD-L1 immune checkpoint blockade, epigenetic modulation thorough bromodomain and extra-terminal (BET) bromodomain inhibition (BBDI), and chemotherapy with paclitaxel that effectively inhibits both primary and metastatic tumor growth in two different syngeneic murine models of TNBC. Detailed cellular and molecular profiling of tumors from single and combination treatment arms revealed increased T- and B-cell infiltration and macrophage reprogramming from MHCII^{low} to a MHCII^{high} phenotype in mice treated with triple combination. Triple combination also had a major impact on gene expression and chromatin profiles shifting cells to a more immunogenic and senescent state. Our results provide strong preclinical evidence to justify clinical testing of BBDI, paclitaxel, and immune checkpoint blockade combination.

Introduction

Breast tumors are highly heterogeneous and are classified on the basis of the expression of estrogen receptor (ER), progesterone receptor (PR), and HER2 into hormone receptor–positive (ER- or PR-positive)/HER2-negative, HER2-positive, and triple-negative (ER-negative, PR-negative, and HER2-negative) subtypes. Tumor progression and response to cancer treatment are determined by both cancer cell-autonomous and microenvironmental factors and mechanistic understanding of the underlying processes is required for the development of rational combination therapies. Combination of chemotherapy with immune checkpoint inhibition (ICI) has demonstrated antitumor activity in triple-negative breast cancer (TNBC) and the PD-1 inhibitor pembrolizumab is currently approved in combination with taxane- or platinum-based chemotherapy as first-line treatment for patients with metastatic PD-L1–positive TNBC (defined as combined positive score ≥10 using the 22C3 pharmDX assay) based on the clinically meaningful improvement in survival observed with the addition of pembrolizumab to chemotherapy compared with placebo plus chemotherapy (1). This benefit was not observed in the PD-L1–negative population, which represents approximately 65% of TNBC, and for most of these patients, chemotherapy remains the standard-of-care. Similarly, the IMPASSION 130 clinical trial reported that combination of atezolizumab (anti-PD-L1) with nab-paclitaxel as first line of treatment in patients with metastatic TNBC prolonged progression-free survival in both the intention-to-treat and PD-L1–positive subgroups (2). However, the follow-up IMPASSION 131 trial testing first-line paclitaxel with or without atezolizumab for unresectable locally advanced/metastatic TNBC did not find differences in survival (3). These contrasting results are potentially due to the use of paclitaxel instead of nanoparticle albumin-bound paclitaxel and the use of steroids that may reduce the efficacy of immunotherapy. Thus, for immunotherapy to be more effective in a larger fraction of TNBC, it is critical to understand the effects of currently available and emerging therapies on the immune microenvironment, identify predictors of response and resistance, and develop rational combinations based on this knowledge.

We previously identified bromodomain and extra-terminal (BET) bromodomain proteins as promising novel therapeutic targets in TNBC (4); however, we also described the rapid emergence of acquired resistance. Thus, subsequently, we conducted genome-wide CRISPR and small-molecule inhibitor screens to identify synthetic lethal combinations with BET bromodomain inhibitors (BBDI; ref. 5). Among others, we found that BBDI synergized with paclitaxel and CDK4/6 inhibitors and this combination overcame resistance to either agent alone, making the clinical translation of these findings a promising avenue to pursue. Several prior publications also reported that PD-L1 is a direct target of BRD4 and BBDIs synergize with ICI therapy in preclinical models (6, 7). Thus, based on our and other's prior results and current clinical treatment options for patients with TNBC, we tested the efficacy of BBDI, paclitaxel, and anti-PD-L1 alone and in dual and triple combinations in preclinical models of TNBC. We found that the triple combination effectively inhibited tumor growth in two different murine models of TNBC, and this was in part driven by increased recruitment of tumor-infiltrating leukocytes, particularly cytotoxic CD8$^+$ T cells and B cells. Our results serve as basis to support the clinical testing of BBDI combinations with ICI and chemotherapy for the treatment of patients with TNBC.

[1]Department of Medical Oncology, Dana-Farber Cancer Institute, Boston, Massachusetts. [2]Department of Medicine, Brigham and Women's Hospital, Boston, Massachusetts. [3]Department of Medicine, Harvard Medical School, Boston, Massachusetts. [4]Harvard University, Cambridge, Massachusetts. [5]Center for Functional Cancer Epigenetics, Dana-Farber Cancer Institute, Boston, Massachusetts. [6]Department of Surgery, Division of Breast Surgery, Brigham and Women's Hospital, Boston, Massachusetts.

Corresponding Author: Kornelia Polyak, Dana-Farber Cancer Institute, 450 Brookline Ave, Boston, MA 02215. E-mail: kornelia_polyak@dfci.harvard.edu

Materials and Methods

Murine mammary tumor cells

MMTV-PyMT cells were derived from a spontaneous tumor in the MMTV-PyMT mammary tumor model, followed by a round of *in vivo* expansion through orthotopic injection in FVB mice. The cells were not cultured, only passaged *in vivo*. EMT-6 cell line was purchased from ATCC (CRL-2755) and cultured in Waymouth's MB 752/1 Medium (Thermo Fisher Scientific, 11220035) with 2 mmol/L L-glutamine and 15% FBS (Sigma-Aldrich, F2442-500ML). The identities of the cell lines were confirmed by short tandem repeat analysis, were regularly tested for *Mycoplasma*, and were used within 10 passages.

BET bromodomain inhibitors

JQ1 was synthesized by J. Qi, as described previously (8), while iBET-762 (GSK525762; ref. 9) was purchased from Selleckchem (catalog no. S7189).

Tumorigenesis studies in mice

All animals were housed and maintained in Dana-Farber Cancer Institute (DFCI) LWC Assessment and Accreditation of Laboratory Animal Care–approved facility. All animal studies were conducted in accordance with the regulations formulated by the Dana-Farber Cancer Institute Animal Care and Use Committee (protocol no. 11-023). Five to 6 weeks old BALBc (Strain #:000651) and FVB/NJ (Strain #:001800) mice were purchased from Jackson Laboratories. FVB mice were injected with 1×10^6 MMTV-PyMT mammary cells, a cell line derived from a spontaneous tumor in the MMTV-PyMT mammary tumor model, followed by a round of *in vivo* expansion through orthotopic injection in FVB mice. Tumors obtained from this expansion were digested into single-cell suspensions and viably frozen. BALBc mice were injected with 200,000 (treatment experiments) or 5×10^5 (comparing cell lines) EMT-6 (ATTC, CRL-2755) mammary tumors cells. Both inguinal mammary fat pads were injected in each mouse. Tumor development was monitored by palpation and once tumors were palpable, usually about 5–7 days after cancer cell inoculation, treatment was initiated. Mice were randomized individually before treatment start. Drugs were administered as single agents or in combination at the following doses: JQ1 at 50 mg/kg by daily gavage, iBET-762 (GSK525762) at 25 mg/kg by daily gavage, anti-PD-L1 antibody (clone 10F.9G2, BioXCell) and paclitaxel each at 10 mg/kg by intraperitoneal injection twice per week. Dose levels and schedules used were chosen based on prior publications. Anti-PD-L1 treatment was started a day later to allow for an initial immune response by the other two treatments. Tumor volumes were measured by caliper every 3 days until the end of the experiment. Measurements were performed by one person throughout the study for consistency and they were not performed in a blinded fashion. Once control tumors reached the study endpoint, all mice were euthanized, and primary tumors and various organs were collected. For the survival analysis using iBET-762, animals were sacrificed once tumor diameter reached 2 cm and/or animals developed poor health or poor body condition. Kaplan–Meier survival analyses were performed by analyzing the dates when tumors became palpable using GraphPad Prism v8 (GraphPad Prism, RRID:SCR_002798). We used 5–10 mice per experimental group as indicated in each experiment.

Tissue processing, histology, and immunofluorescence

Tumors were excised and their weight was recorded. Two small pieces of each tumor were fixed in 10% buffered formalin overnight, stored in 70% ethanol, then paraffin embedded and processed into histologic slides. The remaining fresh tissue was dissociated into single-cell suspension for subsequent FACS analysis and molecular profiling as described previously (10). Briefly, tumors were digested in DMEM/F12 (Thermo Fisher Scientific, MT10090CV) with 2 mg/mL collagenase type 4 (Worthington, LS004189) with constant stirring at 37°C for 1–2 hours. Bone marrow (by flushing the bones), blood, and spleen were also collected and frozen viably in 70% DMEM/10% DMSO/20% FBS for subsequent flow cytometry analysis. Blood was collected in purple-capped K2EDTA-coated tubes (BD Micro-tainer#365974) and mixed immediately to prevent clotting. The samples were then centrifuged at 2,000 RPM for 7 minutes at 4°C. The supernatant (plasma) was transferred to another tube, flash-frozen, and stored at −80°C. Spleens were crushed and cells were strained through a 70-μm cell strainer (Thermo Fisher Scientific #08-771-2). Lungs were excised, washed in PBS, fixed in Bouin Solution overnight, and stored in 70% ethanol. After fixation lungs were inspected for macrometastases followed by paraffin embedding and processing into histologic slides for analysis of micrometastases. Formalin-fixed paraffin-embedded tissues were sectioned and stained with hematoxylin and eosin (H&E). Multicolor immunofluorescence (mIF) analyses were performed as described previously (10). Briefly, tissue was deparaffinized in xylene, put in a series of descending ethanol concentrations (100%, 75%, 50% ethanol), followed by a wash step and heat-induced antigen retrieval in sodium citrate (pH = 6) or TRIS-EDTA buffer (pH = 9). Samples were permeabilized with 0.5% TritonX-100, blocked with 100% goat serum, and stained with antibodies (Supplementary Table S1). For antibodies produced in mice, an additional blocking step was performed with the Mouse-On-Mouse Immunodetection Kit (M.O.M Vector Laboratories). Stained slides were scanned using the Pannoramic MIDI II digital slide scanner (3DHistech), while brightfield images were acquired on a Nikon Ti/E inverted microscope using Nikon Elements software.

Regional lymph nodes adjacent to tumors (on tumor slides) were examined for metastasis by quantifying the area of EPCAM$^+$ cancer cells in the total CD45$^+$ lymph node area. Lung metastasis was quantified by counting lung nodules directly after fixation in Bouin's solution (macrometastases) or after sectioning and H&E staining of the lungs (micrometastases). Tumor cellularity was determined by counting the nuclei using QuPath software QuPath, RRID:SCR_018257; ref. 11) in three random fields/tumor from scanned H&E slides. Tumor cell proliferation was quantified by assessing the number of phospho-histone H3 (pHH3)-positive (mean fluorescence >50 for MMTV-PyMT and >25 for EMT-6) cells as a fraction of all DAPI-stained cells using QuPath software in four random fields/tumor. Cell death was quantified by counting cleaved caspase-3–positive (mean fluorescence >50 for MMTV-PyMT and >75 for EMT-6 tumors) cells as a fraction of all DAPI-stained cells using QuPath software QuPath, RRID:SCR_018257) in two whole slides/tumor. For B-cell quantification, stained slides were scanned, and four random regions per tumor of the same size were created: two at the tumor-stroma interface and two within the tumor. The total DAPI$^+$ tumor cells were quantified for each image and the numbers of B220$^+$ cells were manually counted within each annotation. The fraction of B cells in the tumor and at the tumor-stroma interface was quantified as a percentage of B220$^+$ cells of all DAPI$^+$ cells in the field. For p16 and p21 staining quantification, stained slides were scanned, and the non-necrotic areas of the whole tumors were considered to obtain a fraction of all DAPI-stained cells using QuPath (QuPath, RRID:SCR_018257). Two to three representative areas of each tumor were analyzed to calculate percentage of p16 and p21 double-positive cells.

FACS and flow cytometric analysis

Tumors were harvested and dissociated as described previously (12). Single-cell suspensions were resuspended in PBE [PBS with 0.5% BSA and 2 mmol/L ethylenediaminetetraacetic acid (EDTA)] and incubated at 4°C for 30 minutes with antibodies (Supplementary Table S1). Flow cytometric analysis was carried out on an LSR Fortessa Flow Cytometer (BD Biosciences) and data were analyzed using the FlowJo cell analysis software (FlowJo, LLC, RRID:SCR_008520). Cells were sorted using BD FACSAria II SORP UV (Becton Dickinson).

Mouse cytokine array

Cytokine array was performed using Proteome Profiler Mouse XL Cytokine Array Kit (R&D Systems, ARY028) following the manufacturer's protocol. Briefly, tumors were homogenized and lysed in PBS containing 1% Triton X-100 and protease inhibitors. Protein concentrations were quantified using Bradford BSA assay and 200 μg protein lysate evenly were pooled from nine (vehicle) and eight (triple combination) tumors of each group. Dot blots were quantified using ImageJ (ImageJ, RRID:SCR_003070) and normalized to the intensity of three independent reference controls.

RNA sequencing experiment and analysis

Dissociated EMT-6 tumors collected at 15 days after injection to mice were separated into CD45$^+$ and CD45$^-$ cell fractions using anti-CD45 antibody (BioLegend, catalog no. 103102) coupled to Dynabeads (Life Technologies, 10004D) to enrich for leukocytes and tumor cells, respectively. Cells were counted and about 50,000 cells for each fraction were frozen for bulk Assay for Transposase-Accessible Chromatin using sequencing (ATAC-seq). The remaining cells were used for RNA extraction and bulk RNA sequencing (RNA-seq). Total RNA was extracted using the RNeasy Mini Kit (Qiagen). The total RNA was measured by Agilent 2100 Bioanalyzer. RNA-seq libraries were prepared using Clontech Low Input mRNA Library (Clontech SMARTer) v4 kit from less than 10 ng of purified total RNA according to the manufacturer's protocol. The concentrations of finished double-stranded DNA library were measured by Qubit Fluorometer, the size of library fragment was measured by Agilent TapeStation 2200 (Agilent TapeStation Laptop, RRID:SCR_019547), and qRT-PCR for adapted library molar concentration measurement according to manufacturer's protocols. Uniquely indexed libraries were pooled in equimolar ratios and sequenced on an Illumina NextSeq500 with Paired-End reads by the DFCI Molecular Biology Core Facilities. RNA-seq datasets were aligned to the mouse reference genome mm9. VIPER pipeline was used for data processing, and genes with constant 0 counts across all samples were filtered out. Principal component analysis (PCA) was performed using edgeR (RRID:SCR_012802) package with "PC1" and "PC2" computed by "prcomp" function. Enrichment analysis for JQ1 response and resistance signatures from human SUM159 cell line (4) and Sensecence_TP53_Target_UP signature (MSigDB: M6171) were calculated using "GSVA" package. Differentially expressing genes (DEG) were calculated using DESeq2 package with a cutoff of $P_{adj} < 0.05$ and |log$_2$Fold Change|>1. Heat maps of DEGs were plotted using "ComplexHeatmap" package. Pathway analyses were performed by input the DEGs into MSigDB webportal and significantly enriched pathways with FDR < 0.05 were selected under REACTOME (CD45$^-$ cells) and ImmuneSig (CD45$^+$ cells) gene set collections. Relative crosstalk scores (RCS) were calculated essentially as described previously (13). Ligand-receptor pairs showing no expression in either CD45$^-$ or CD45$^+$ cells were filtered out. Delta RCS values were calculated by subtract the RCS of vehicle group from one of the treatment groups. T-cell and B-cell repertoires were inferred using TRUST4 algorithm by extracting CDR3 regions reads from BAM files of CD45$^+$ cells. Diversity scores were calculated using "immunarch" package.

ATAC-seq experiment and data analysis

ATAC-seq was performed following the previously describe Omni-ATAC protocol (14). Briefly, viably frozen cells were pelleted by centrifugation and cell counts and viability was checked using Countess cell counter and NucBlue stain. A total of 200,000 cells were resuspended in 1 mL of ice-cold ATAC-seq resuspension buffer (RSB; 10 mmol/L Tris-HCl pH 7.4, 10 mmol/L NaCl, and 3 mmol/L MgCl$_2$ in water). Cells were centrifuged at 800 relative centrifugal force (r.c.f.) for 5 minutes in a prechilled (4°C) fixed-angle centrifuge and the supernatant was carefully aspirated by pipetting. Cell pellets were resuspended in 50 μL of ATAC-seq RSB containing 0.1% NP40, 0.1% Tween-20, and 0.01% digitonin by pipetting gently and incubated on ice for 3 minutes. To stop lysis, 1 mL of ATAC-seq RSB containing 0.1% Tween-20 (without NP40 or digitonin) was added and tubes were inverted to mix. Nuclei were then centrifuged for 10 minutes at 800 r.c.f. in a prechilled (4°C) fixed-angle centrifuge. Supernatant was removed and nuclei were resuspended in 50 μL of transposition mix (25 μL 2× TD buffer, 2.5 μL transposase Tn5 (Illumina 20034197), 16.5 μL PBS, 0.5 μL 1% digitonin, 0.5 μL 10% Tween-20, and 5 μL water) by pipetting gently. Transposition reactions were incubated at 37°C for 30 minutes in a thermomixer at 1,000 revolutions per minute (r.p.m.). Reactions were cleaned up with Qiagen MinElute kit. Library prep was done with qPCR optimization as described previously (15). Amplified libraries were purified with Qiagen Qiaquick PCR purification columns as per the kit instructions and were quantified using Qubit.

Peak calling and data analysis

All samples were processed through the computational pipeline developed at the DFCI Center for Functional Cancer Epigenetics using primarily open-source programs (16, 17). Sequence tags were aligned with Burrows-Wheeler Aligner (18) to build mm9 and uniquely mapped, non-redundant reads were retained. These reads were used to generate binding sites with Model-Based Analysis of ChIP-Seq 2 (MACS v2.1.1.20160309), with a q-value (FDR) threshold of 0.01 (19). We evaluated multiple quality control criteria based on alignment information and peak quality: (i) sequence quality score; (ii) uniquely mappable reads (reads that can only map to one location in the genome); (iii) uniquely mappable locations (locations that can only be mapped by at least one read); (iv) peak overlap with Velcro regions, a comprehensive set of locations—also called consensus signal artifact regions—in the genome that have anomalous, unstructured high signal or read counts in next-generation sequencing experiments independent of cell line and of type of experiment; (v) number of total peaks (the minimum required was 10,000); (vi) high-confidence peaks (the number of peaks that are 10-fold enriched over background); (vii) percentage overlap with known DHS sites derived from the ENCODE Project (the minimum required to meet the threshold was 80%); and (viii) peak conservation (a measure of sequence similarity across species based on the hypothesis that conserved sequences are more likely to be functional).

Differential binding analyses

Peaks from all samples were merged to create a union set of sites for each transcription factor and histone mark using bedops (20). Sample-sample correlation and differential peaks analysis were performed by the CoBRA (COBrA, RRID:SCR_005677) pipeline (17). Read densities were calculated for each peak for each sample and used for the

comparison of cistromes across samples. Sample similarity was determined by hierarchical clustering using the Spearman correlation between samples. Differential peaks were identified by DEseq2 (DESeq2, RRID:SCR_015687) with adjusted $P \leq 0.05$. A total number of reads in each sample was applied to the size factor in DEseq2, which can normalize the sequencing depth between samples. Peaks from each group were used for motif analysis using AME function in MEME Suit with cut-off E-value $\leq$ 1e-10. E-value represents estimate of the number of motifs (with the same width and number of occurrences) that would have equal or higher log likelihood ratio if the input sequences had been generated randomly according to the (zero-order portion of the) background model. Binding and expression target analysis (BETA) was performed to determine the association between differential ATAC sites and DEGs from RNA-seq with $-/+$ 100 kb of transcription start site as the defined distance. Peaks visualization in genomic tracks was performed using WashU Epigenome Browser (https://epigenomegateway.wustl.edu/).

Statistical analyses

Significance of results was determined using unpaired two-tailed Student t tests with Welch correction, unless otherwise noted. $P < 0.05$ was defined as statistically significant. Error bars indicate SEM unless otherwise noted.

Study approval

All animal studies described were carried out under protocol 11-023 approved by the Dana-Farber Cancer Institute Animal Care and Use Committee.

Data availability

The RNA-seq and ATAC-seq datasets have been deposited to Gene Expression Omnibus with the accession number GSE229428.

Results

Effect of combined BET and PD-L1 inhibition with paclitaxel on mammary tumor growth

To test whether the addition of BET bromodomain inhibitors (e.g., JQ1; ref. 8) improves the efficacy of PD-L1 blockade (anti-PD-L1) and chemotherapy (paclitaxel), mouse mammary tumor cells were implanted orthotopically into mammary fat pads of syngeneic mice and subject to treatment once tumors were palpable (Fig. 1A). We tested two different syngeneic mammary tumor models, a MMTV-PyMT cell line derived through *in vivo* expansion of a mammary tumor from MMTV-PyMT transgenic mouse and the EMT-6 mammary tumor cell line (Fig. 1B and C). MMTV-PyMT is commonly used as a preclinical model of TNBC, while the EMT-6 cell line we chose due to its favorable features for immunotherapy studies characterized by significantly higher frequency of $CD45^+$ leukocytes and trends of higher T and B cells abundance within tumors (Supplementary Fig. S1A and S1B). Treatments were well tolerated, and animal weight remained similar across all the treatment groups (Supplementary Fig. S1C). Tumors in mice treated with single agents grew slower compared with vehicle control, although this was significant only for JQ1 at the experimental endpoint in the MMTV-PyMT model ($P = 3 \times 10^{-8}$ for tumor volume, $P = 2 \times 10^{-5}$ for tumor weight; Fig. 1B). Among dual combinations, JQ1+paclitaxel showed the highest efficacy with significant reduction in tumor volume ($P = 2 \times 10^{-8}$ in MMTV-PyMT, $P = 0.023$ in EMT-6) and weight ($P = 3 \times 10^{-8}$ in MMTV-PyMT, $P = 3 \times 10^{-4}$ in EMT-6) in both models (Fig. 1B and C) consistent with our prior data using xenografts

in immunodeficient mice (5, 21). Anti-PD-L1+paclitaxel was slightly more effective than either monotherapy, while the triple combination showed the most prominent inhibition of tumor growth compared with vehicle in both models resulting in significantly smaller tumor volumes ($P = 3 \times 10^{-10}$ for MMTV-PyMT and $P = 7 \times 10^4$ for EMT-6), and tumor weight ($P = 4 \times 10^{-10}$ for MMTV-PyMT and $P = 2 \times 10^{-4}$ for EMT-6; Fig. 1B and C; Supplementary Fig. S1D and S1E).

Triple combination treatment also significantly decreased metastasis to regional lymph nodes in the MMTV-PyMT model compared with vehicle controls ($P = 2.5 \times 10^{-3}$; Fig. 1D). Similarly, the number of micrometastatic lesions in the lungs of mice with EMT-6 tumors was significantly lower in triple combination–treated animals compared with vehicle controls ($P = 0.0352$; Fig. 1E). The effect of single agents and dual combinations on lymph node and lung metastasis could not be evaluated quantitatively due to low sample size. Taken together, these data show that the triple combination of BBDI, anti-PD-L1, and paclitaxel is effective in reducing primary tumor growth and metastasis in murine models of TNBC.

The impact of treatment on cell proliferation and apoptosis

To explore potential mechanisms underlying the observed treatment-induced reduction in tumor growth, we first assessed tumor cell content, proliferation, and apoptosis. Analysis of H&E-stained tumor sections revealed that triple combination and even some dual combinations and single agents significantly reduced tumor cell cellularity in both models (Fig. 1F; Supplementary Fig. S1F). We also analyzed cell proliferation based on immunofluorescence for pHH3, a G_2–M cell-cycle phase-specific marker, and detected a significant decrease in the relative fraction of $pHH3^+$ cells in tumors from mice treated with JQ1 ($P = 9 \times 10^{-7}$), anti-PD-L1 ($P = 0.042$), JQ1+anti-PD-L1 ($P = 0.003$), anti-PD-L1+paclitaxel ($P = 0.010$), and triple combination ($P = 0.036$) compared with controls in the MMTV-PyMT model (Fig. 1G and H). In contrast, the fraction of $pHH3^+$ cells was increased in paclitaxel and JQ1+paclitaxel treated tumors consistent with paclitaxel inducing a G_2–M arrest leading to accumulation of $pHH3^+$ cells (Fig. 1G and H). In the EMT-6 model, the frequency of $pHH3^+$ cells was low (<1%) in most tumors, making quantification challenging, but there was a significant ($P = 0.018$) decrease in JQ1-treated tumors compared with controls (Supplementary Fig. S1G). The frequency of cleaved caspase-3–positive apoptotic cells was less than 5% in most cases, with high variability among tumors with significant increase ($P = 0.023$) compared with control observed only in JQ1+anti-PD-L1–treated EMT-6 tumors (Supplementary Fig. S1H). In contrast, there were significantly fewer cleaved caspase-3–positive cells in several treatment groups relative to controls, including anti-PD-L1 ($P = 0.025$), JQ1+paclitaxel ($P = 4 \times 10^{-6}$), and triple combination ($P = 2 \times 10^{-5}$) in MMTV-PyMT tumors possibly due to the faster growth of control tumors compared with treated ones, leading to increased cell death and necrosis (Supplementary Fig. S1I).

BBDI, anti-PD-L1, and paclitaxel combination leads to tumor regression and prolongs survival

To validate our results with a different BBDI and to assess the effects of long-term treatment on overall survival, we repeated our experiment using the EMT-6 model and Molibresib (GSK525762; iBET-762) a compound with improved pharmacokinetic properties that was in clinical trial at the time we performed the experiments (9). Similar to results with JQ1, the triple combination of BBDI, anti-PD-L1, and paclitaxel showed significant reduction in primary tumor growth compared with vehicle over the first 12 days of treatment
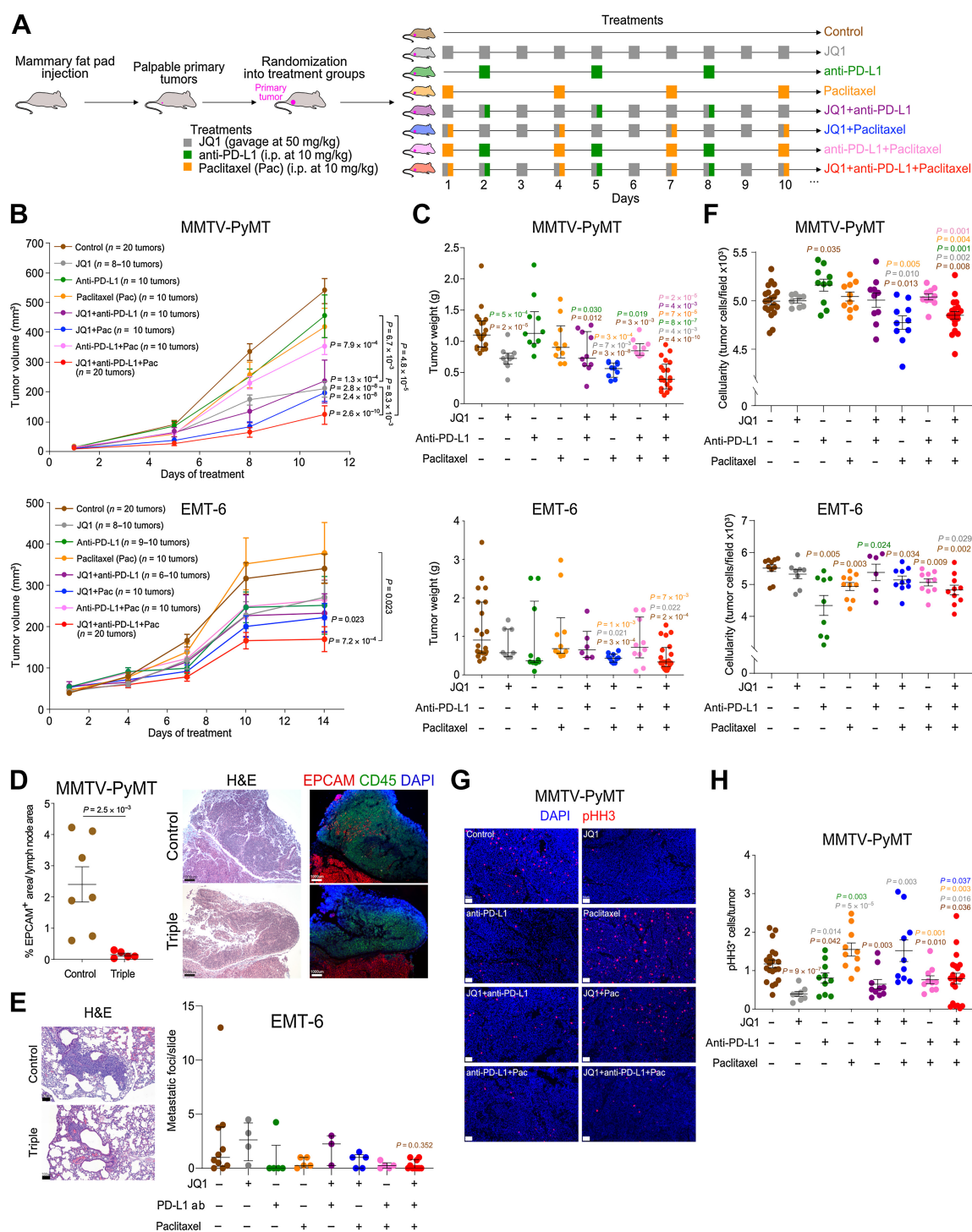
Figure 1.
Triplet combination of anti-PD-L1, JQ1, and paclitaxel reduces breast cancer progression and metastasis in two murine models. **A,** Schematic showing experimental set-up of *in vivo* drug treatment experiments. Tumor volumes during the experiment (**B**) and tumor weights (**C**) at experimental endpoint of orthotopically implanted MMTV-PyMT and EMT-6 mammary tumors. Drug treatments were initiated when tumors were palpable (day 1). **D,** Quantification of EPCAM⁺ area and representative H&E-stained and fluorescent images of EPCAM⁺ cancer cells in regional lymph nodes of MMTV-PyMT tumors from mice treated with vehicle or triple combination (JQ1+anti-PD-L1+paclitaxel). **E,** Lung metastasis of EMT-6 mammary tumor cells treated with indicated treatments. Representative H&E images display metastatic lesions in the lung. **F,** Quantification of cellularity of MMTV-PyMT and EMT-6 mammary tumors. Representative immunofluorescence images (**G**) and quantification (**H**) of tumor cell proliferation at experimental endpoints of MMTV-PyMT tumor experiments. Scale bars, 50 μm. *P* values: two-sided *t* test with Welch correction (**B, C, F**); two-tailed Mann–Whitney test (**C, E, H**). Colors of *P* values in **C, F,** and **H** indicate the groups compared (e.g., brown marks difference relative to vehicle).
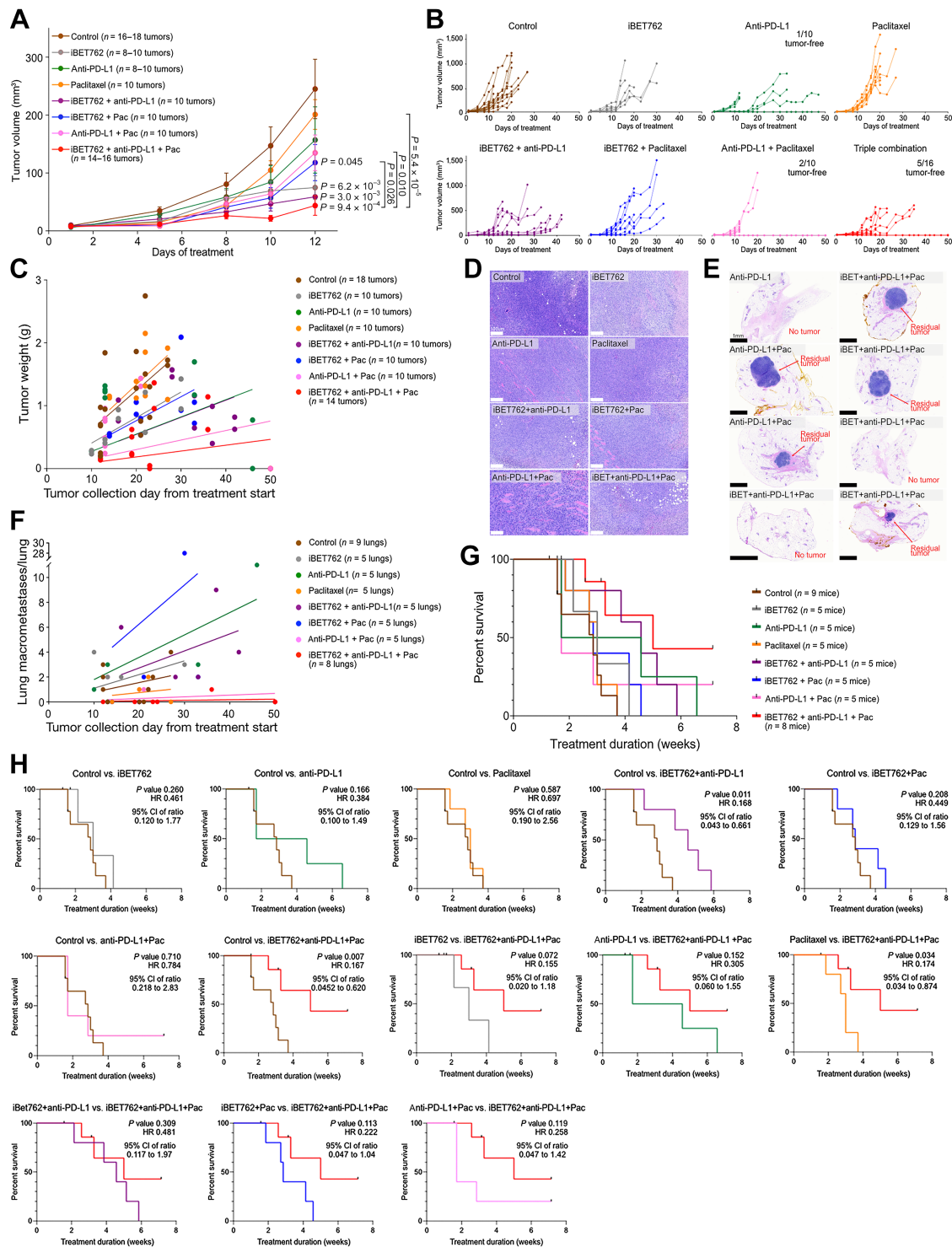
Figure 2.
The effect of treatment on survival and tumor growth and metastasis. Tumor volumes shown as averages per timepoint until day 12 posttreatment start (**A**) or for all mice in each group for the entire duration of the study (**B**). Mice without tumors are shown for the applicable groups. *P* values were calculated by two-sided *t* test with Welch correction. **C,** Tumor weight displayed on day it was collected relative to treatment start. Shown are linear regressions. H&E staining of tumors (**D**) and tumor-free mammary fat pads of animals whose tumors showed complete regression (**E**). Red arrows mark residual microscopic tumors in some mammary glands. **F,** Lung macrometastatic lesions were quantified and correlated with the day on which lungs were collected. Shown are linear regressions. Survival analysis of all groups (**G**) and each group compared with control (top row) or the triplet combination (bottom row; **H**). HRs and log-rank *P* values are shown. log-rank test for all eight groups to derive a multiple looks statistical evaluation detected a significant difference in at least one group (*P* = 0.0097).

$(P = 9.4 \times 10^{-4})$ without affecting mouse body weight (**Fig. 2A**; Supplementary Fig. S2A—S2D). However, in contrast to JQ1, iBET-762 administered as single agent $(P = 6.2 \times 10^{-3})$ or in combination with anti-PD-L1 $(P = 3.0 \times 10^{-3})$ or paclitaxel $(P = 0.045)$ also significantly reduced tumor volume after short-term treatment, presumably due to its better pharmacodynamic properties compared with JQ1 (**Fig. 2A**). Thus, at these early timepoints, we did not observe a significant difference in tumor volume between triple combination and iBET-762 alone or in combination with anti-PD-L1. Unlike in the previous experiments, mice were only sacrificed when they reached the experimental endpoint (defined by tumor diameter of 2 cm and/or poor body condition), allowing us to evaluate the long-term effects of treatment. Even with prolonged long-term treatment, the triple combination of iBET-762, anti-PD-L1, and paclitaxel lead to the most significant reduction in tumor growth compared with vehicle (**Fig. 2B–E**). At the experimental endpoint several mice in multiple treatment groups were completely tumor-free due to treatment-induced tumor regression (5/16 of triple combination, 1/10 of anti-PD-L1, 2/10 of anti-PD-L1+paclitaxel; **Fig. 2B–E**), highlighting the effectiveness of combination immunotherapy.

Analysis of the lungs showed a significant reduction in lung macrometastases in the triple combination treated cohort compared with the vehicle control animals $(P = 0.0263$; **Fig. 2F**), even though most control animals were sacrificed much earlier than treated ones. The iBET+anti-PD-L1 treatment group had significantly $(P = 0.032)$ higher frequency of lung macrometastases compared with controls while other treatment groups did not show significant differences.

Finally, we analyzed the overall survival of animals and found that animals treated with iBET-762+anti-PD-L1 $(P = 0.011$, HR: 0.168) and the triple combination $(P = 0.007$, HR: 0.167) showed a significant increase in survival compared with vehicle control and paclitaxel only groups (**Fig. 2G** and **H**). Interestingly, while single-agent anti-PD-L1 treatment only modestly reduced tumor growth at earlier timepoints (e.g., day 12), anti-PD-L1 combination treatment groups showed improved survival compared with both control and single agents and BBDI+paclitaxel combination. Taken together, these results further demonstrate the efficacy of BBDI, anti-PD-L1, and paclitaxel triple combination to reduce both primary and metastatic tumor growth and prolong survival, with 31% (5/16) of tumors showing complete regression by endpoint.

Treatment-associated differences in the immune microenvironment

We next examined the effect of treatments on leukocyte infiltration into tumors by performing polychromatic flow cytometry for immune cells of the lymphoid and myeloid lineages (Supplementary Fig. S3A). We found significant treatment-associated differences in immune cell composition in both tumor models, with many shared and some model-specific changes (**Fig. 3A–G**; Supplementary Fig. S3B and S3C; Supplementary Table S2). In the MMTV-PyMT model, the relative fraction of total CD45$^+$, B220$^+$ B cells, and CD4$^+$ T cells was generally higher in most treatment groups relatively to control with the highest fraction observed with triple combination, but due to the variability among tumors within group the observed differences were not always statistically significant (Supplementary Fig. S3B). However, there was a significant inverse correlation between the relative fraction of each of these three cell populations and primary tumor weight when all tumors combined (Supplementary Fig. S3C). Within T cells, the relative fraction of CD8$^+$ cytotoxic T and CD4$^+$ T$_H$ cells was higher in treatment groups including JQ1, with most pronounced increase observed with triple combination (**Fig. 3C**). We also observed that

macrophages shifted from having a predominantly MHCII^{low} protumorigenic phenotype to an antitumorigenic MHCII^{high} phenotype (**Fig. 3D**).

In the EMT-6 model, we also saw an expansion of B cells in most treatment groups compared with vehicle control (**Fig. 3B**), and the fraction of CD3$^+$ T cells, and total CD8$^+$ and activated cytotoxic CD69$^+$CD8$^+$ T cell increased significantly in mice that received the triple combination treatment compared with controls and even when compared with some single and dual combinations (**Fig. 3E** and **F**). Furthermore, the relative fraction of total CD3$^+$ and CD8$^+$ cells showed significant inverse correlation with primary tumor weight when all tumors combined (**Fig. 3G**). Similar to the MMTV-PyMT tumors, the relative frequency of macrophages with antitumorigenic MHCII^{high} phenotype increased compared with those with MHCII^{low} phenotype following treatment compared with controls and this was the most significant with JQ1+pac dual combination (**Fig. 3H**).

Overall, all treatments had some impact on tumor-infiltrating immune cell populations, and in general dual and triple combinations had stronger effects than single agents. These findings demonstrate that adding BBDI to anti-PD-L1 antibody and paclitaxel combination shifts the tumor immune microenvironment toward a more active antitumor phenotype, which may explain the observed reduction in tumor growth and increase in survival.

Changes in tumor-infiltrating immune cell spatial patterns

Immune cell localization within tumors is also an important determinant of antitumor immune responses and it also impacts the efficacy of immunotherapies (22). Thus, we performed mIF to analyze the localization of CD45$^+$ leukocytes, B220$^+$ B cells, and CD3$^+$ T cells within tumors. In the MMTV-PyMT model, we detected significantly more CD45$^+$ leukocytes at the tumor-stroma interface in mice treated with triple combination compared with vehicle controls (control 6% vs. combination 20%, $P = 0.025$; **Fig. 3I**). However, the fraction of CD45$^+$ cells within tumors was only slightly increased with triple combination compared with control (control 1% vs. combination 2%, $P = 0.115$). In contrast, the fraction of B220$^+$ B cells at the tumor-stromal interface was not different between vehicle and the triple combination–treated tumors, but there was a significant increase in tumor-infiltrating B220$^+$ B cells in both the MMTV-PyMT and EMT-6 models (**Fig. 3J** and **K**; Supplementary Fig. S3D and S3E). Mono and dual therapies had varying effects on the B-cell infiltration in the two tumor models at different locations. But, overall B-cell frequencies were significantly lower compared with controls in most mono and dual combination-treated groups (**Fig. 3J** and **K**). In contrast, the relative frequencies of CD3$^+$ T cells did not show significant differences between vehicle-treated and triple combination–treated groups, although there was higher frequency of CD3$^+$ T cells at the tumor-stroma interface in both MMTV-PyMT and EMT-6 models (Supplementary Fig. S3F and S3G).

Treatment-associated differences in gene expression profiles

To assess gene expression changes associated with treatment, we performed RNA-seq on tumor leukocyte-enriched (CD45$^+$) and epithelial/stromal cell–enriched (CD45$^-$) populations purified using magnetic beads from EMT-6 tumors from mice treated with JQ1, and dual and triple combinations including JQ1 (i.e., JQ1+paclitaxel, JQ1+anti-PD-L1, and triple combination; **Fig. 4A**). PCA revealed a distinct segregation of the CD45$^+$ and CD45$^-$ cell populations (**Fig. 4B**, All cells). Known immune cell (e.g., *Ptprc*, *Cd68*, and *H2-AA*) and known epithelial (e.g., *Krt8* and *Krt18*) and stromal markers (e.g., *Col1a1*, *Acta2*, and *Thbs2*) were significantly higher in CD45$^+$
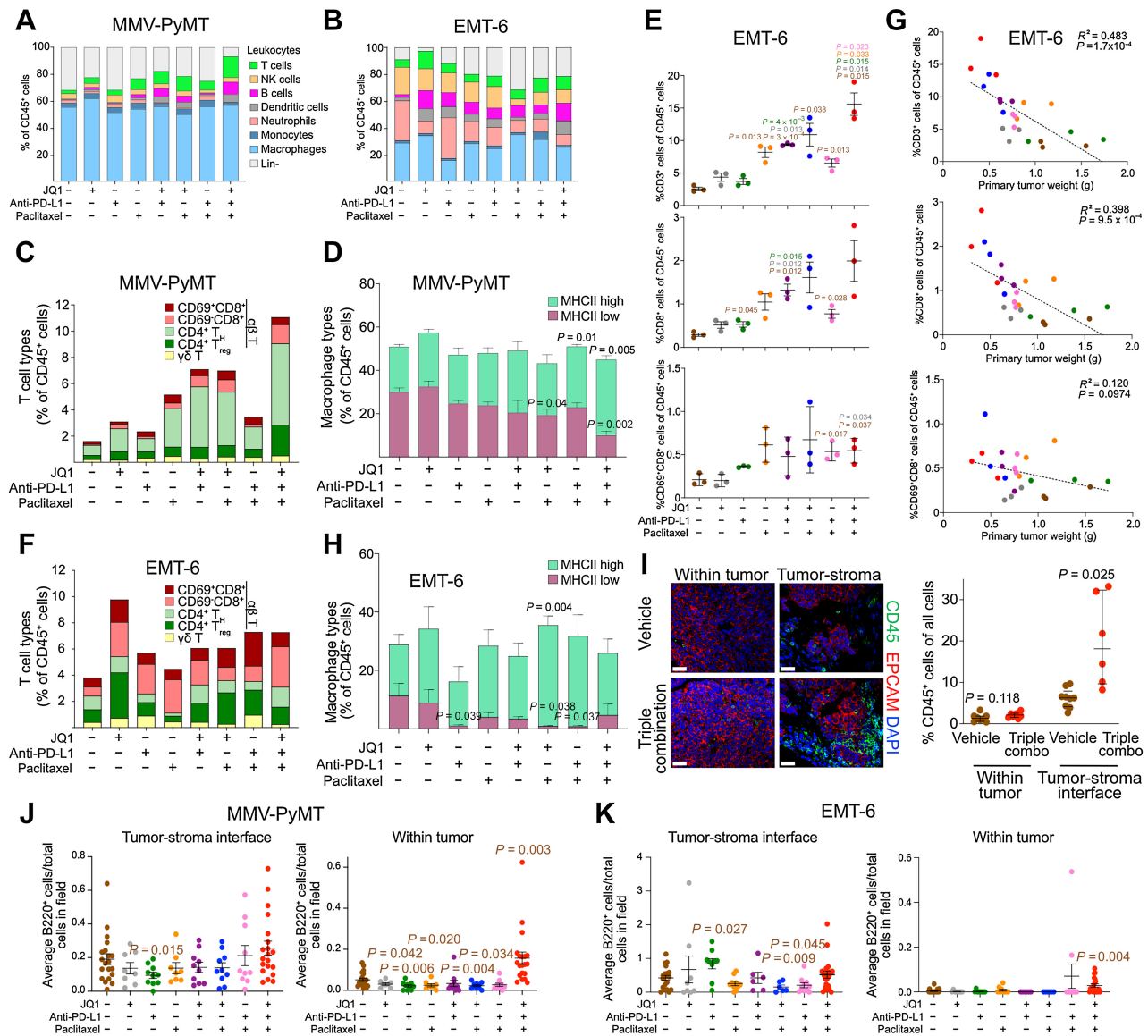
Figure 3.
Changes in the tumor immune microenvironment. Stacked bar plots depicting flow cytometric analysis of immune cell populations in MMTV-PyMT (**A**) and EMT-6 (**B**) mammary tumors from animals with the indicated treatment. Stacked bar plots illustrating flow cytometric analysis of T-cell subpopulations (**C**) and macrophages (**D**) in MMTV-PyMT mammary tumors from animals with the indicated treatment. **E,** Plots depicting treatment-related differences in total $CD3^+$, $CD8^+$, and activated $CD69^+CD8^+$ T cells quantified by flow cytometry in EMT-6 mammary tumors. **F,** Stacked bar plots illustrating flow cytometric analysis of T-cell subpopulations in MMTV-PyMT mammary tumors from animals with the indicated treatment. **G,** Plots depicting correlation of tumor weight with relative frequencies of total $CD3^+$, $CD8^+$, and activated $CD69^+CD8^+$ T cells quantified by flow cytometry in EMT-6 mammary tumors. Correlations of a subset of T-cell populations with tumor weight are shown using linear regression and statistics are calculated by Pearson correlation. **H,** Stacked bar plots illustrating flow cytometric analysis of macrophages in EMT-6 mammary tumors from animals with the indicated treatment. **I,** Quantification, and representative images of $CD45^+$ immune cells in control and triplet combination-treated MMTV-PyMT tumors located inside the tumor or at tumor-stroma interface. Quantification of B-cell frequency ($B220^+$) in tumors and at the tumor-stroma interface of MMTV-PyMT (**J**) and EMT-6 (**K**) tumors. P values were calculated by two-sided t test with Welch correction in all panels. Colors of P values in **E, G, J,** and **K** indicate the groups compared (e.g., brown marks difference relative to vehicle).

and $CD45^-$ cells, respectively (Supplementary Fig. S4A). In line with this, unsupervised clustering of hallmark pathways demonstrated enrichment of proliferation and immune-related gene signatures in $CD45^-$ and $CD45^+$ populations, respectively (Supplementary Fig. S4B). Furthermore, PCAs on $CD45^-$ or $CD45^+$ cells alone showed good clustering and high relatedness of samples from the same treatment groups, with $CD45^+$ cells showing more variability poten-

tially due to $CD45^+$ cells being a mixture of multiple immune cell types (**Fig. 4B**). The JQ1+anti-PD-L1 groups were more similar to vehicle in both $CD45^-$ and $CD45^+$ cell populations, whereas JQ1 and JQ1+paclitaxel groups were more distinguished (**Fig. 4B**). To determine whether JQ1-induced gene expression patterns are conserved across species and cell types, we assessed the enrichment of our prior gene signatures derived from human TNBC cell line SUM159 and its JQ1-
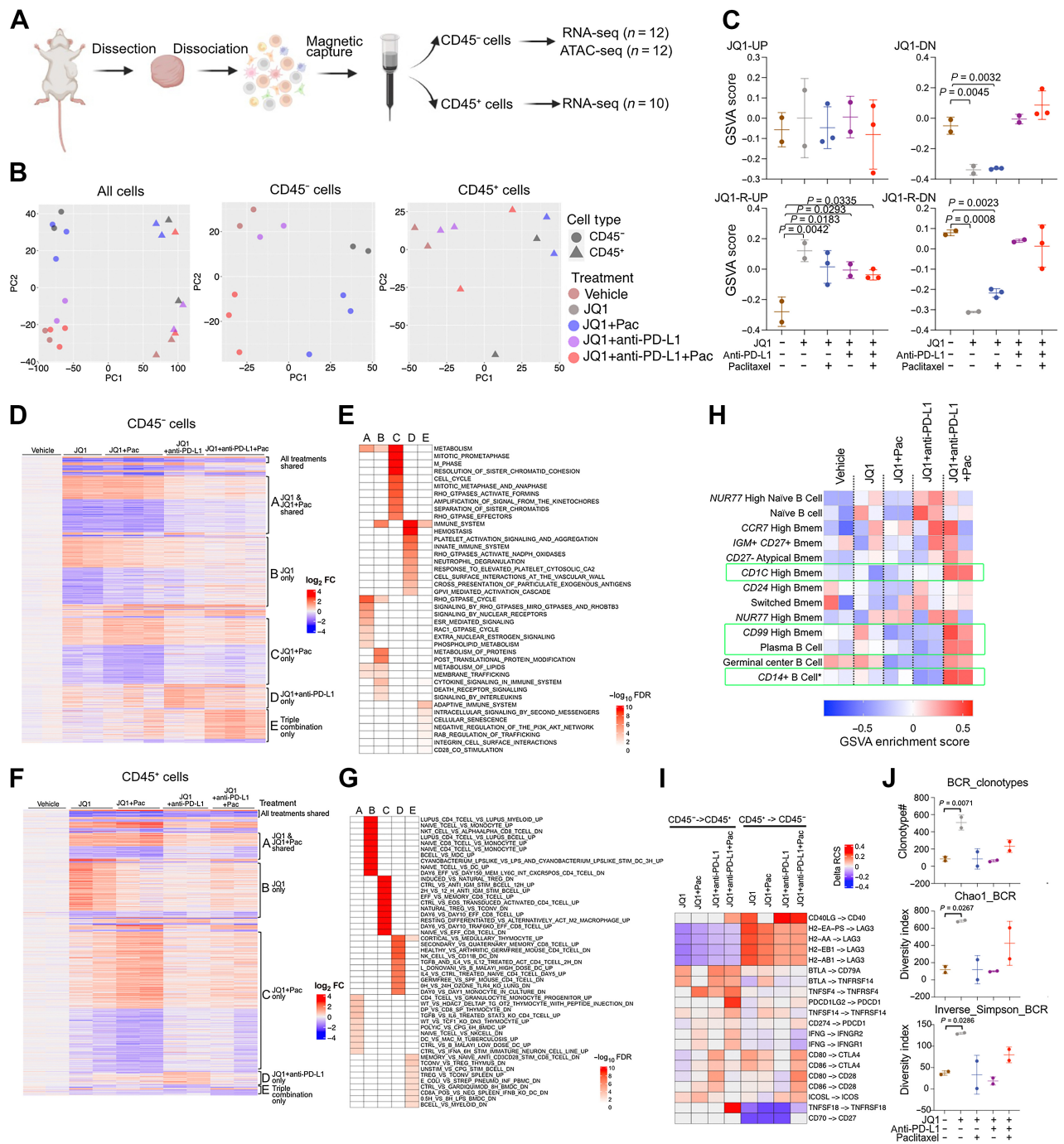
Figure 4.
Tumor and immune cell RNA-seq profiles. **A,** Schematic outline of RNA-seq and ATAC-seq profiling of CD45^{-} and CD45^{+} cells purified from EMT6 tumors. **B,** PCA plot depicting the segregation of all (left), CD45^{-} only (middle), and CD45^{+} only (right) samples by treatments. **C,** Dot plot showing the enrichment scores with mean ± SD of the indicated gene signatures in CD45^{-} cell RNA-seq data. JQ1-UP and JQ1-DN: genes upregulated and downregulated, respectively, by JQ1 in SUM159 human TNBC cell line; JQ1-R-UP and JQ1-R-DN: genes upregulated and downregulated, respectively, in JQ1-resistant compared with parental SUM159 cells. Heat maps illustrating union of DEGs from all the treatments compared with vehicle group in CD45^{-} (**D**) and CD45^{+} (**F**) cells. Major DEG clusters are highlighted. **E–G,** Heat maps depicting of significantly (FDR < 0.05) enriched pathways in each DEG cluster in **D** and **F**. Reactome and ImmuneSig DB signature collections were applied to RNA-seq data from CD45^{-} (**E**) and CD45^{+} (**G**) cells, respectively. **H,** Heat map showing the enrichment scores of 13 TNBC-specific B-cell subtypes in RNA-seq data from CD45^{+} cells of each treatment group. * marks cells with both B cell and monocyte features, likely representing Cd14^{+} monocytes that phagocytosed B cells. **I,** Heat map illustrating the RCS changes of 20 immune checkpoint ligand-receptor pairs between each treatment and vehicle group. **J,** Dot plots showing BCR clonotype and diversity indexes with mean ± SD derived from CD45^{+} cell RNA-seq data from all treatment groups. P values were calculated using two-sided Student t test (**C, I**).

resistant derivative (4). We found that genes downregulated by short-term JQ1 treatment in SUM159 cells had significantly reduced expression in JQ1 and JQ1+paclitaxel-treated EMT6 tumor-derived CD45$^-$ cells (**Fig. 4C**). In contrast, the gene expression patterns of all treatment groups were more similar to JQ1-resistant SUM159 cell transcriptomes with JQ1 and JQ1+paclitaxel showing the strongest shift (**Fig. 4C**). These results suggest that residual tumors after 14 days treatment of mice are enriched for treatment-resistant cancer cells.

Next, we identified genes significantly differentially expressed in pairwise comparisons between vehicle and each of the treated groups as well as between triple combination and JQ1 and double combinations (Supplementary Table S3). In both CD45$^-$ and CD45$^+$ cells, comparison of JQ1 and JQ1+paclitaxel groups with vehicle had the highest number of DEGs with more downregulated genes in CD45$^-$ and more upregulated genes in the CD45$^+$ populations, suggesting different roles for BRD4 in regulating tumor epithelial and immune cell expression patterns (Supplementary Fig. S4C). In contrast, DEGs between vehicle versus JQ+anti-PD-L1 or triple combinations were fewer with more upregulated than downregulated genes in CD45$^-$ cells (Supplementary Fig. S4C).

We further interrogated DEGs in both CD45$^-$ (tumor-enriched) and CD45$^+$ (immune-enriched) cell populations. In CD45$^-$ cells, the majority of DEGs (60%) were unique to individual treatment groups with only 34 genes being commonly altered by all treatments (**Fig. 4D**). We classified the DEGs into five broader clusters (**Fig. 4D**; Supplementary Table S3). Clusters A, B, and C were derived from JQ1 and JQ1+paclitaxel groups with 30% of DEGs common between them. Many of these shared genes (Cluster A) are involved in Rho/Rac GTPase pathway and lipid metabolism, whereas DEGs unique to JQ1 (Cluster B) were functionally similar but also included protein metabolism and cytokine regulation-related genes (**Fig. 4E**). DEGs unique to JQ1+paclitaxel (Cluster C) had predominantly cell cycle–related and mitosis-related functions, while JQ1+anti-PD-L1 (Cluster D) unique DEGs were enriched in immune-related functions including innate immune system and antigen presentation. Genes unique to the triple combination (Cluster E) also showed enrichment in immune-related pathways like adaptive immune system in addition to cellular senescence and negative regulation of PI3K/AKT (**Fig. 4E**).

Analysis of the predicted transcriptional regulators of DEGs by epigenetic Landscape In Silico deletion Analysis (LISA) (23) revealed that BRD4 was significantly associated only with JQ1-induced unique differences, while other treatments showed other predicted regulators, including the STAT4 and STAT5 transcription factors in the triple combination group (Supplementary Fig. S4D). In sum, these analyses suggested that the changes occurring in CD45$^-$ cell populations upon JQ1 and JQ1+paclitaxel treatment are mainly cell-autonomous (e.g., cell cycle–related), while dual and triple combinations including anti-PD-L1 have more non–cell-autonomous (e.g., immune-related) functional impact.

The DEGs in the CD45$^+$ cells also segregated into five broader clusters, but the functional annotation of each cluster was largely distinguished (**Fig. 4F** and **G**; Supplementary Table S4). DEGs derived from JQ1 treatment alone (Cluster B) mainly linked to naïve CD4$^+$ and CD8$^+$ T cell functions, while JQ1+paclitaxel unique genes (Cluster C) were associated with increased effector CD8$^+$ T cell and decreased regulatory T cell (Treg) functions implying immune activation. JQ1+anti-PD-L1 treatment-associated program (Cluster D) was related to IL4-treatment–like CD4$^+$ T-cell changes as well as secondary CD8$^+$ T-cell response. Finally, the triple combination (Cluster E) affected CD28/CD3-relevant CD8$^+$ T-cell and Treg functions. Given our observation of significantly increased intratumor B cells in

the triple combination group (**Fig. 3J** and **K**), we further examined TNBC-specific B-cell subtype abundance using cell type–specific gene signatures derived from single-cell RNA-seq data (24). We found specific enrichment in triple combination group for *Cd1c* high memory, *Cd99* high memory, germinal center, and plasma B cells, and a small subpopulation positive for both B-cell markers and *Cd14* likely represent CD14$^+$ monocytes that phagocytosed B cells (**Fig. 4H**), suggestive of locally ongoing class switch recombination and somatic hypermutations in potential tertiary lymphoid structures as well as more pronounced antibody production.

Analysis of upstream regulators of DEGs in CD45$^+$ cells by LISA (23) pointed out several epigenetic regulators such as JARID2, CHD8, and BAZ1A in triple combination-unique program (Supplementary Fig. S4E), implying epigenetic reprogramming. JARID2 is a component of the PRC2 complex with essential roles in TCR-mediated T-cell activation (25), while BAZ1A is a BET bromodomain protein related to BRD4 and a master regulator of pan-HDAC inhibitor panobinostat-induced cellular senescence program in neuroblastoma (26).

Predicted cellular interactions based on expression profiles

Our spatial analysis of immune cell topology suggested a more pronounced immune activation at the tumor-stroma interface in triple combination–treated tumors, which led us to infer signaling cross-talk between tumor and immune components and the impact of treatment on these. We utilized a recently described mathematical model, RCS (13), and we computed tumor-to-tumor, tumor-to-immune, immune-to-tumor, and immune-to-immune RCSs based on the expression of 690 ligand-receptor pairs from our RNA-seq data. We found that the tumor epithelial/stromal (CD45$^-$ cells) component was a more predominant signaling sender to both itself and also to immune (CD45$^+$) cells (Supplementary Fig. S4F). Interrogating 20 immune checkpoint ligand-receptor pairs in more detail, we found an increase in inhibitory immune checkpoint signaling by triple combination in CD45$^-$ cells including PD-L2-PD1 and TNFSF18-TNFRSF18 (**Fig. 4I**). In line with CD45$^+$ cell transcriptional profiles (**Fig. 4G**, Cluster E), enhanced CD28-CD80 and CD28-CD86 stimulatory program was more prominently present in triple combination CD45$^+$ group implying enhanced cytotoxic T-cell activity (**Fig. 4I**). Analysis of a larger set of ligand-receptor pairs highlighted a strong enrichment of ephrin signaling in two-way tumor/stroma and immune cell cross-talk in the triple combination group (Supplementary Fig. S4G), serving as another potential nexus in immune activation (27).

Finally, inference of TCR and B-cell repertoire (BCR) clonotype repertoire from CD45$^+$ cell RNA-seq data using TRUST4 algorithm (28) showed a significant increase in BCR clonotypes and diversity upon JQ1 treatment (**Fig. 4J**), which is consistent with the increase in B cells we detected by flow cytometry in both MMTV-PyMT and EMT6 models (**Fig. 3A** and **B**). TCR clonotypes showed a similar, but not significant, trend (Supplementary Fig. S4H). These data suggest that JQ1 treatment leads to an expansion of immune repertoire and a more active immune environment that enhances the efficacy of anti-PD-L1 immune checkpoint inhibitor therapy.

Treatment-induced changes in chromatin patterns

Next, we performed ATAC-seq on CD45$^-$ cells to analyze treatment-induced changes in chromatin patterns. Similar to the RNA-seq data, we found good clustering based on treatment condition using PCA (**Fig. 5A**), and we observed similar trends as in the RNA-seq data: JQ1 and JQ1+paclitaxel samples clustered together, triple combination–treated samples were more unique, while control and
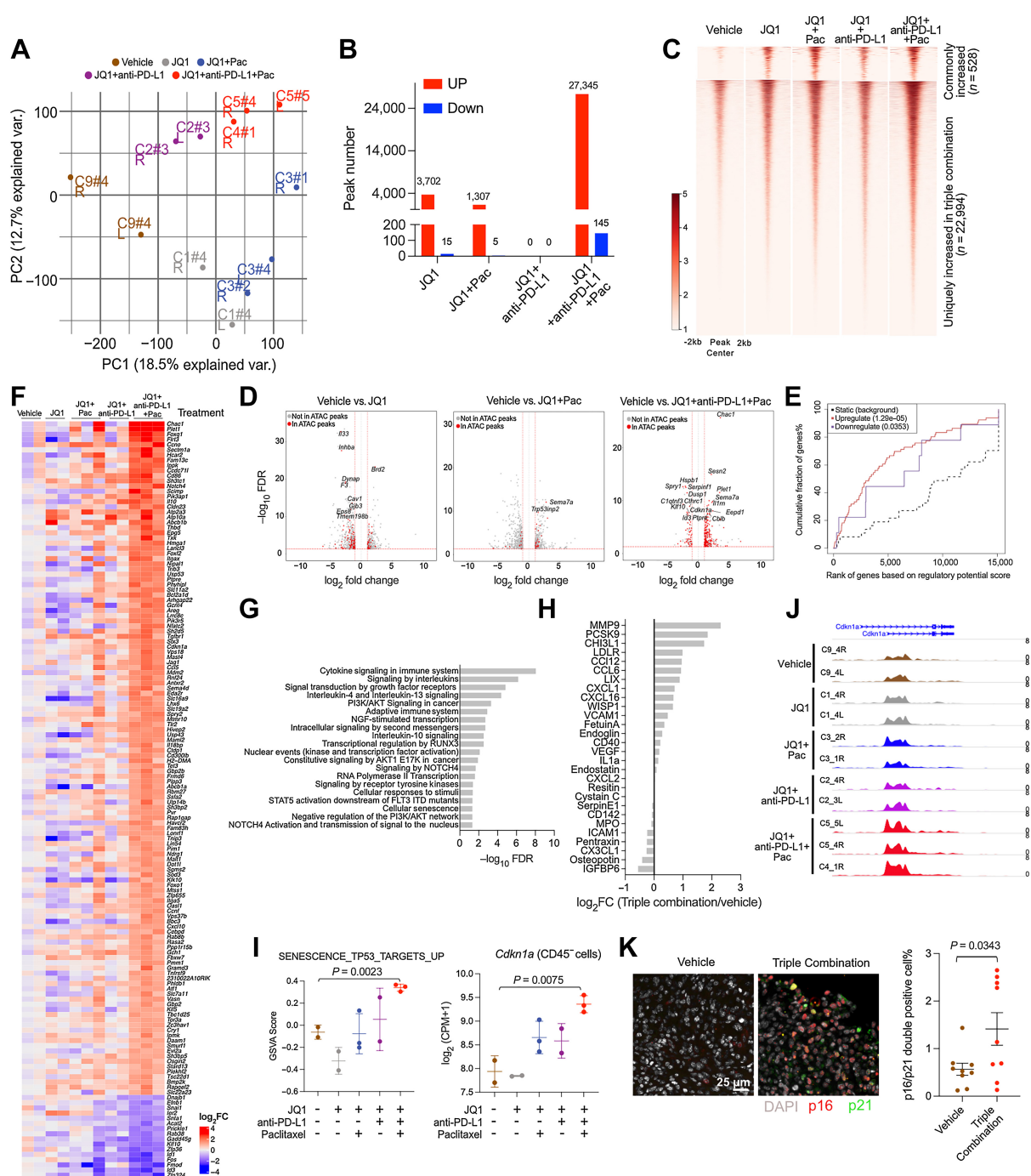
Figure 5.
CD45⁻ cell ATAC-seq profiles. **A,** PCA plot depicting the distribution of CD45⁻ cells by ATAC-seq signal. **B,** Bar plot showing accessible chromatin sites significantly different in each treatment group compared with vehicle. **C,** Heat map illustrating ATAC signal of peaks increased by all treatment or unique to triple combination. One representative sample from each group was used for the visualization. **D,** Volcano plots showing DEGs in CD45⁻ cells between vehicle and JQ1, JQ1+paclitaxel, or triple combination groups. DEGs associated with increased ATAC sites are highlighted in red. **E,** Line plot showing the association of DEGs unique to the triple combination group with the corresponding increased ATAC sites. **F,** Heat map illustrating DEGs associated with increased ATAC sites uniquely induced by triple combination treatment. **G,** Bar plot depicting the significantly (FDR < 0.05) enriched Reactome pathways derived from genes in **F**. **H,** Bar plot showing the fold changes of all detectable cytokines in tumors from mice treated with triple combination normalized to vehicle-treated tumors. **I,** Dot plot showing the enrichment scores of a senescence signature and *Cdkn1a* in CD45⁻ cell RNA-seq data. *P* values were calculated using two-sided Student *t* test. **J,** Genomic tracks of ATAC-seq signal at *Cdkn1a* locus across in the indicated samples. **K,** Immunofluorescence analysis of p16 and p21 in vehicle and triple combination–treated EMT-6 tumors. Representative images (left) and dot plot (right) depicting the relative fraction of p16 and p21 double-positive cells in each individual tumor. Numbers were calculated from average of two to three representative areas of each tumor (*n* = 9 for each group). *P* values were calculated using two-sided Student *t* test (**I, K**).

JQ1+anti-PD-L1clustered closer to each other (**Fig. 5A**). Analysis of differential peaks compared with vehicle group demonstrated more up than down peaks with the triple combination–treated group showing seven to 20 times more differential peaks than the JQ1 alone and JQ1+paclitaxel groups, suggesting that it leads to wide opening of the chromatin (**Fig. 5B**; Supplementary Table S5). Consistent with the PCA plot, no significantly changed ATAC peaks were detected in JQ1+anti-PD-L1 group.

Genomic regions in the triple combination treatment–induced gained ATAC sites showed higher baseline accessibility compared with those induced in other treatment groups, suggesting that triple combination mainly expanded the already open chromatin rather than open up new regions (**Fig. 5C**). Integration of differential ATAC peaks and DEGs from RNA-seq revealed that 67% triple combination–induced DEGs were associated with increased ATAC sites, including *Chac1* and *Sesn2*, the topmost upregulated genes in triple combination–treated group (**Fig. 5D**). Interesting, both *Chac1* and *Sesne2* are stress-inducible genes: *Chac1* is an ATF4 target gene involved in unfolded protein response (29), while *Sesn2* is induced by hypoxia (30). In contrast, only 18.4% and 7.3% DEGs were associated with differential ATAC sites in the JQ1 and JQ1+paclitaxel groups, respectively (**Fig. 5D**). The significant association between triple combination–induced changes in chromatin and gene expression patterns was also confirmed by BETA (31), with a more significant association observed for upregulated genes (**Fig. 5E**), while no association was detected in JQ1 and JQ1+paclitaxel groups (Supplementary Fig. S5A).

Analysis of sequence motifs significantly enriched in these increased ATAC sites showed the highest number of motifs (299) in triple combination and motifs enriched in JQ1 and JQ1+paclitaxel treatment groups were all a subset of these 299 (Supplementary Fig. S5B; Supplementary Table S6). STAT5A/B and MAF are among the 89 motifs uniquely enriched in triple combination (Supplementary Fig. S5B) and they were also identified as unique upstream regulators by LISA analysis of DEGs (Supplementary Fig. S4D), implying these two transcription factors are recruited to these open chromatin regions and regulate gene expression patterns. Overall, these results demonstrate distinct modes of gene regulation between triple combination and single- or dual-agent treatments wherein the triple combination remarkably reshapes the chromatin while others mostly regulate genes at the transcriptional level.

Given that the majority of triple combination–related DEGs were associated with gained ATAC sites, we next dissected the potential functional output of 147 (131 up and 16 down) DEGs linked to gained ATAC sites exclusively regulated in the triple combination group (**Fig. 5F**). Pathway enrichment analysis identified cytokine signaling, PI3K/AKT pathway, cellular senescence and STAT5 activation linked to these genes (**Fig. 5G**). Cytokine array analysis confirmed the upregulation of numerous cytokines in triple combination tumors compared with vehicle including CCL12 (orthologous to human CCL2 and CCL8), CCL6 (orthologous to human CCL23), CXCL1, and CXCL16 (**Fig. 5H**). We and others previously reported that JQ1 induces cellular senescence associated with increased *CDKN1A* (p21) expression (4). Here, while no effects were observed with JQ1 treatment alone, the triple combination induced a p53-driven senescence program with a strong increase of *Cdkn1a* (p21) expression (**Fig. 5I**). We also observed an increase in chromatin accessibility at the *Cdkn1a* genomic locus in tumors treated with triple combination (**Fig. 5J**). Immunofluorescence analysis also demonstrated a significant increase in the fraction of p21 and p16 double-positive cells in triple combination–treated tumors (**Fig. 5K**). In conclusion, these results suggest senescence as an outcome of epigenetic reprogramming induced by the triple combination, which might contribute to the immune-related changes and tumor suppression.

Discussion

Breast cancer has been relatively not responsive to immune check-point inhibitors in part due to low tumor mutation burden, high degree of aneuploidy, and limited infiltration of T cells, especially in ER-positive tumors (32). Even in TNBC where anti-PD1 has been approved in combination with paclitaxel for patients with PD-L1–positive tumors, durable responses have been observed only in a subset of cases necessitating the development of novel therapeutic strategies (33). We and others have previously described that combination of BBDIs with chemotherapy (e.g., paclitaxel) or targeted therapies (e.g., CDK4/6 inhibitors) increases efficacy and decreases therapeutic resistance (4, 5, 21, 34). We observed particularly strong synergy between BBDIs and paclitaxel and CDK4/6 inhibitors; agents already in use for breast cancer treatment facilitating clinical translation. In this study, we describe the preclinical evaluation of BBDI (JQ1 and iBET-762), paclitaxel, and anti-PD-L1 triple combination using the MMTV-PyMT and EMT-6 murine mammary tumor models of TNBC. We found that the triple combination effectively reduced tumor growth and prolonged survival. Our comprehensive cellular and molecular profiling of the tumors revealed BBDI-induced changes in both cancer cells and the immune environment that could explain the enhanced efficacy of immunotherapy. Specifically, we detected significant increase in intratumor immune cell population, especially T and B cells, by FACS and immunofluorescence, and an overall shift to a more antitumor immune environment.

Several prior studies have reported that combining BBDIs with immune checkpoint inhibitors increases the efficacy of immunotherapy through multiple different mechanisms. Treatment of human prostate cancer cell lines with JQ1 decreased PD-L1 expression and upregulated MHC-I expression increasing antigen presentation and making cancer cells more susceptible to killing by cytotoxic CD8+ T cells in cell culture assays (35). In line with this, combination of JQ1 with anti-CTLA-4 increased intratumoral CD8+ T cells in the My-CAP model of prostate cancer, but it was not more effective to control tumor growth than anti-CTLA-4 alone (35). In contrast, in the *KRAS*-mutant non–small cell lung cancer model the JQ1 and anti-PD-1 combination was more efficacious than either agent alone and this was associated with a decrease in tumor-infiltrating Tregs and activation of CD4+ Th1 T cells (36). Similar findings were reported for JQ1 and anti-PD1 combination in colorectal cancer models (37), while in TH-MYCN transgenic mouse model of neuroblastoma JQ1 increased the fraction of PD1+ T cells and enhanced the efficacy of anti-PD-1 treatment (38). Improved efficacy was also reported for JQ1 and anti-PD-L1 combination in hepatocellular carcinoma due to increased CD8+ T-cell activation and upregulation of PD-L1 expression (39).

In our study, we tested two different BBDIs (JQ1—a tool compound and GSK525762/iBET-762—a clinical-grade compound) in two different preclinical models of TNBC (MMTV-PyMT and EMT6) and compared dual combination of BBDI with paclitaxel or anti-PD-L1 as well as triple combination treatment. We found in both models that short-term JQ1+paclitaxel treatment significantly reduced tumor growth compared with vehicle control and that the triple combination treatment was not significantly better compared with these dual agents. However, the triple combination was the most effective in prolonging

survival and inducing complete regression of these aggressively growing tumors, significantly more effective than paclitaxel+anti-PD-L1 treatment that is currently approved therapy for a subset of patients with TNBC. The triple combination treatment also induced similar changes in the immune environment in both models characterized by increased T- and B-cell infiltration and shift of macrophages from MHC-II low to MHC-II high profiles. In contrast, BCR clonotype repertoire was most significantly increased in the JQ1 alone treatment group compared with control implying specific effects on B cells. While some of these immune changes may lead to improved response to anti-PD-L1 treatment, others may reflect resistance mechanisms. For example, B cells can have both positive and negative effects on response to ICI and clinical outcome, depending on the particular cancer type and specific B-cell subtypes involved (40–42). Like in melanoma, plasmablast-like B cells improve response to anti-PD-1 therapy and patient survival (40). In our RNA-seq data of CD45$^+$ cells, we observed significant enrichment for $Cd1c$ high memory, $Cd99$ high memory, germinal, and plasma B cells, which may reflect the presence of tertiary lymphoid structures and increased antibody production or immune activation within tumors. Interestingly, the strongest enrichment in the triple combination was for $Cd14^+$ cells with B-cell features that likely represent CD14$^+$ monocytes that phagocytosed B cells potentially implying increased phagocytosis in triple combination–treated tumors. Our observation that the changes in these B-cell subpopulations are specific for the triple combination implies that B cells may particularly be important to induce tumor regression and prolong survival in this model.

Further analysis of CD45$^-$ (tumor cell-enriched) and CD45$^+$ (immune cell-enriched) gene expression profiles revealed numerous changes that could activate antitumor immune responses. While immune-related gene signatures were upregulated in CD45$^-$ cells not only by the triple combination treatment, but also by JQ1 and JQ1+anti-PD-L1 treatments, only the triple combination group showed enrichment for adaptive immune response and T-cell activation. Because RNA-seq was performed on residual tumors after treatment, some of the expression changes may reflect resistance mechanisms instead of predictors of response. In line with this, our RNA-seq profiling of tumor epithelial cells in the EMT-6 model showed upregulation of JQ1 resistance–associated gene signatures in all treatment groups compared with vehicle control. Because senescence is a major feature of JQ1 resistance, this may indicate treatment-induced senescence of cancer cells.

In addition to expression changes, we also observed a significant increase in open chromatin regions by ATAC-seq in CD45$^-$ cells isolated from JQ1, JQ1+paclitaxel, and triple combination treated mice, with the most pronounced differences observed with the triple combination. Integrated analysis of CD45$^-$ cell RNA-seq and ATAC-seq data revealed significant increase in senescence pathways and cytokine signaling, which can contribute to increased immune cell infiltration and changes in the immune environment. Senescent cancer cells have been shown to be immunogenic and rewire the tumor immune environment increasing the efficacy of antitumor immune responses (43, 44). In line with this, our analysis of tumor cytokine levels showed significant elevation of several chemokines, including CXCL1 and CXCL16, which can induce senescence (45) and enhance T-cell infiltration (46), respectively.

In summary, our data provide strong preclinical rational for combining BBDI with paclitaxel and ICI in patients with TNBC to improve treatment efficacy. Thus, we designed a phase Ib clinical trial to test this combination, specifically Molibresib, atezolizumab, and nab-paclitaxel in patients with locally advanced or metastatic TNBC based on the data

described in this article. However, while our study was in progress, there were numerous changes in BBDIs in clinical development due to results of early-stage trials. Molibresib (iBET-762) was discontinued because of high frequency of adverse events and lack of meaningful response rates as single agent (47). Similarly, the RO6870810 program was terminated by Roche due to toxicity issues (48, 49). Meanwhile, Trotabresib (BMS-986158) has been developed and recent data indicate exceptional responses in patients with BRD4-NUTM1 NUT carcinoma harboring a BRD4 splice site mutation (50). Currently, ZEN-3694, an orally bioavailable BBDI with favorable pharmacokinetic and toxicity profile is being evaluated in clinical trials for prostate cancer (51) and TNBC (52) in combination with enzalutamide and talazoparib, respectively, with promising results. Main adverse events reported for BBDIs in clinical trials include fatigue, thrombocytopenia, taste alteration, and visual changes described with ZEN-3694. Fatigue and thrombocytopenia overlap with expected toxicities of nab-paclitaxel; pembrolizumab can also cause fatigue. However, these adverse events are likely to be manageable by adjusting dosing schedules. Therefore, we changed our trial design and have initiated a phase Ib clinical trial (CTEP 10525) to test this combination, specifically ZEN-3694, pembrolizumab, and nab-paclitaxel in patients with locally advanced or metastatic TNBC. But, the BBDI landscape is rapidly evolving and new generation of BBDIs are being developed that specifically target the BD1 or BD2 domains, or have bifunctional properties (i.e., also inhibit certain kinases) or act as degraders (53). One of the limitations of BBDIs, and epigenetic therapies in general, has been their limited efficacy as single agents. However, due to the importance of epigenetic state switching in therapeutic resistance, agents targeting epigenetic regulators may only be effective in combinations, necessitating a change in how novel compounds are evaluated in clinical trials. Our preclinical results showing high efficacy of BBDI, paclitaxel, and anti-PD-L1 triple combination is an example for this and likely there will be many more.

Authors' Disclosures

Authors' Contributions

M. Alečković: Conceptualization, formal analysis, investigation, writing–original draft. **Z. Li:** Formal analysis, writing–original draft. **N. Zhou:** Formal analysis. **X. Qiu:** Formal analysis. **B. Lulseged:** Investigation. **P. Foidart:** Data curation. **X.-Y. Huang:** Investigation. **K. Garza:** Investigation. **S. Shu:** Investigation. **N. Kesten:** Formal analysis. **R. Li:** Formal analysis. **K. Lim:** Investigation. **A.C. Garrido-Castro:** Writing–original draft. **J.L. Guerriero:** Investigation. **J. Qi:** Investigation. **H.W. Long:** Supervision. **K. Polyak:** Conceptualization, resources, supervision, funding acquisition, writing–original draft, project administration, writing–review and editing.

Acknowledgments

Note

Supplementary data for this article are available at Molecular Cancer Therapeutics Online (http://mct.aacrjournals.org/).

References

1. Cortes J, Cescon DW, Rugo HS, Nowecki Z, Im SA, Yusof MM, et al. Pembrolizumab plus chemotherapy versus placebo plus chemotherapy for previously untreated locally recurrent inoperable or metastatic triple-negative breast cancer (KEYNOTE-355): a randomised, placebo-controlled, double-blind, phase 3 clinical trial. Lancet 2020;396:1817–28.

2. Kagihara JA, Andress M, Diamond JR. Nab-paclitaxel and atezolizumab for the treatment of PD-L1-positive, metastatic triple-negative breast cancer: review and future directions. Expert Rev Precis Med Drug Dev 2020;5:59–65.

3. Miles D, Gligorov J, Andre F, Cameron D, Schneeweiss A, Barrios C, et al. Primary results from IMpassion131, a double-blind, placebo-controlled, randomised phase III trial of first-line paclitaxel with or without atezolizumab for unresectable locally advanced/metastatic triple-negative breast cancer. Ann Oncol 2021;32:994–1004.

4. Shu S, Lin CY, He HH, Witwicki RM, Tabassum DP, Roberts JM, et al. Response and resistance to BET bromodomain inhibitors in triple-negative breast cancer. Nature 2016;529:413–7.

5. Shu S, Wu HJ, Ge JY, Zeid R, Harris IS, Jovanovic B, et al. Synthetic lethal and resistance interactions with BET bromodomain inhibitors in triple-negative breast cancer. Mol Cell 2020;78:1096–113.

6. Zhu H, Bengsch F, Svoronos N, Rutkowski MR, Bitler BG, Allegrezza MJ, et al. BET bromodomain inhibition promotes anti-tumor immunity by suppressing PD-L1 expression. Cell Rep 2016;16:2829–37.

7. Hogg SJ, Vervoort SJ, Deswal S, Ott CJ, Li J, Cluse LA, et al. BET-Bromodomain inhibitors engage the host immune system and regulate expression of the immune checkpoint ligand PD-L1. Cell Rep 2017;18:2162–74.

8. Filippakopoulos P, Qi J, Picaud S, Shen Y, Smith WB, Fedorov O, et al. Selective inhibition of BET bromodomains. Nature 2010;468:1067–73.

9. Zhao Y, Yang CY, Wang S. The making of I-BET762, a BET bromodomain inhibitor now in clinical development. J Med Chem 2013;56:7498–500.

10. Huh SJ, Clement K, Jee D, Merlini A, Choudhury S, Maruyama R, et al. Age- and pregnancy-associated DNA methylation changes in mammary epithelial cells. Stem Cell Rep 2015;4:297–311.

11. Bankhead P, Loughrey MB, Fernandez JA, Dombrowski Y, McArt DG, Dunne PD, et al. QuPath: open source software for digital pathology image analysis. Sci Rep 2017;7:16878.

12. Gil Del Alcazar CR, Trinh A, Aleckovic M, Rojas Jimenez E, Harper NW, Oliphant MU, et al. Insights into immune escape during tumor evolution and response to immunotherapy using a rat model of breast cancer. Cancer Immunol Res 2022;10:680–97.

13. Ghoshdastider U, Rohatgi N, Mojtabavi Naeini M, Baruah P, Revkov E, Guo YA, et al. Pan-cancer analysis of ligand-receptor cross-talk in the tumor microenvironment. Cancer Res 2021;81:1802–12.

14. Corces MR, Trevino AE, Hamilton EG, Greenside PG, Sinnott-Armstrong NA, Vesuna S, et al. An improved ATAC-seq protocol reduces background and enables interrogation of frozen tissues. Nat Methods 2017;14:959–62.

15. Buenrostro JD, Wu B, Chang HY, Greenleaf WJ. ATAC-seq: a method for assaying chromatin accessibility genome-wide. Curr Protoc Mol Biol 2015;109: 21.29.1–9.

16. Taing L, Cousins C, Bai G, Paloma C, Qiu X, Brown M, et al. CHIPS: a snakemake pipeline for quality control and reproducible processing of chromatin profiling data. F1000Research 2021;10:517.

17. Qiu X, Feit AS, Feiglin A, Xie Y, Kesten N, Taing L, et al. CoBRA: containerized bioinformatics workflow for reproducible ChIP/ATAC-seq analysis. Genomics Proteomics Bioinformatics 2021;19:652–61.

18. Li H, Durbin R. Fast and accurate short read alignment with Burrows-Wheeler transform. Bioinformatics 2009;25:1754–60.

19. Zhang Y, Liu T, Meyer CA, Eeckhoute J, Johnson DS, Bernstein BE, et al. Model-based analysis of ChIP-Seq (MACS). Genome Biol 2008;9:R137.

20. Neph S, Kuehn MS, Reynolds AP, Haugen E, Thurman RE, Johnson AK, et al. BEDOPS: high-performance genomic feature operations. Bioinformatics 2012; 28:1919–20.

21. Ge JY, Shu S, Kwon M, Jovanovic B, Murphy K, Gulvady A, et al. Acquired resistance to combined BET and CDK4/6 inhibition in triple-negative breast cancer. Nat Commun 2020;11:2350.

22. Tooley KA, Escobar G, Anderson AC. Spatial determinants of CD8(+) T cell differentiation in cancer. Trends Cancer 2022;8:642–54.

23. Qin Q, Fan J, Zheng R, Wan C, Mei S, Wu Q, et al. Lisa: inferring transcriptional regulators through integrative modeling of public chromatin accessibility and ChIP-seq data. Genome Biol 2020;21:32.

24. Hu Q, Hong Y, Qi P, Lu G, Mai X, Xu S, et al. Atlas of breast cancer infiltrated B-lymphocytes revealed by paired single-cell RNA-sequencing and antigen receptor profiling. Nat Commun 2021;12:2186.

25. Dobenecker MW, Park JS, Marcello J, McCabe MT, Gregory R, Knight SD, et al. Signaling function of PRC2 is essential for TCR-driven T cell responses. J Exp Med 2018;215:1101–13.

26. Milazzo G, Perini G, Giorgi FM. Single-cell sequencing identifies master regulators affected by panobinostat in neuroblastoma cells. Genes 2022;13: 2240.

27. Darling TK, Lamb TJ. Emerging roles for Eph receptors and ephrin ligands in immunity. Front Immunol 2019;10:1473.

28. Song L, Cohen D, Ouyang Z, Cao Y, Hu X, Liu XS. TRUST4: immune repertoire reconstruction from bulk and single-cell RNA-seq data. Nat Methods 2021;18: 627–30.

29. Mungrue IN, Pagnon J, Kohannim O, Gargalovic PS, Lusis AJ. CHAC1/ MGC4504 is a novel proapoptotic component of the unfolded protein response, downstream of the ATF4-ATF3-CHOP cascade. J Immunol 2009;182:466–76.

30. Budanov AV, Sablina AA, Feinstein E, Koonin EV, Chumakov PM. Regeneration of peroxiredoxins by p53-regulated sestrins, homologs of bacterial AhpD. Science 2004;304:596–600.

31. Wang S, Sun H, Ma J, Zang C, Wang C, Wang J, et al. Target analysis by integration of transcriptome and ChIP-seq data with BETA. Nat Protoc 2013;8: 2502–15.

32. Debien V, De Caluwe A, Wang X, Piccart-Gebhart M, Tuohy VK, Romano E, et al. Immunotherapy in breast cancer: an overview of current strategies and perspectives. NPJ Breast Cancer 2023;9:7.

33. Jacobs F, Agostinetto E, Miggiano C, De Sanctis R, Zambelli A, Santoro A. Hope and hype around immunotherapy in triple-negative breast cancer. Cancers 2023; 15:2933.

34. Halder TG, Soldi R, Sharma S. Bromodomain and extraterminal domain protein bromodomain inhibitor based cancer therapeutics. Curr Opin Oncol 2021;33: 526–31.

35. Mao W, Ghasemzadeh A, Freeman ZT, Obradovic A, Chaimowitz MG, Nirschl TR, et al. Immunogenicity of prostate cancer is augmented by BET bromodomain inhibition. J Immunother Cancer 2019;7:277.

36. Adeegbe DO, Liu S, Hattersley MM, Bowden M, Zhou CW, Li S, et al. BET bromodomain inhibition cooperates with PD-1 blockade to facilitate antitumor response in Kras-mutant non-small cell lung cancer. Cancer Immunol Res 2018; 6:1234–45.

37. Wang H, Liu G, Jin X, Song S, Chen S, Zhou P, et al. BET inhibitor JQ1 enhances anti-tumor immunity and synergizes with PD-1 blockade in CRC. J Cancer 2022; 13:2126–37.

38. Sauvage D, Bosseler M, Viry E, Kanli G, Oudin A, Berchem G, et al. The BET protein inhibitor JQ1 decreases hypoxia and improves the therapeutic benefit of anti-PD-1 in a high-risk neuroblastoma mouse model. Cells 2022; 11:2783.

39. Liu C, Miao X, Wang Y, Wen L, Cheng X, Kong D, et al. Bromo- and extraterminal domain protein inhibition improves immunotherapy efficacy in hepatocellular carcinoma. Cancer Sci 2020;111:3503–15.

40. Griss J, Bauer W, Wagner C, Simon M, Chen M, Grabmeier-Pfistershammer K, et al. B cells sustain inflammation and predict response to immune checkpoint blockade in human melanoma. Nat Commun 2019;10:4186.

41. Petitprez F, de Reynies A, Keung EZ, Chen TW, Sun CM, Calderaro J, et al. B cells are associated with survival and immunotherapy response in sarcoma. Nature 2020;577:556–60.

42. Kim SS, Sumner WA, Miyauchi S, Cohen EEW, Califano JA, Sharabi AB. Role of B cells in responses to checkpoint blockade immunotherapy and overall survival of cancer patients. Clin Cancer Res 2021;27:6075–82.

43. Chen HA, Ho YJ, Mezzadra R, Adrover JM, Smolkin R, Zhu C, et al. Senescence rewires microenvironment sensing to facilitate antitumor immunity. Cancer Discov 2023;13:432–53.

44. Marin I, Boix O, Garcia-Garijo A, Sirois I, Caballe A, Zarzuela E, et al. Cellular senescence is immunogenic and promotes antitumor immunity. Cancer Discov 2023;13:410–31.

45. Acosta JC, O'Loghlen A, Banito A, Raguz S, Gil J. Control of senescence by CXCR2 and its ligands. Cell Cycle 2008;7:2956–9.

46. Mabrouk N, Tran T, Sam I, Pourmir I, Gruel N, Granier C, et al. CXCR6 expressing T cells: functions and role in the control of tumors. Front Immunol 2022;13:1022136.

47. Cousin S, Blay JY, Garcia IB, de Bono JS, Le Tourneau C, Moreno V, et al. Safety, pharmacokinetic, pharmacodynamic and clinical activity of molibre-sib for the treatment of nuclear protein in testis carcinoma and other cancers: results of a phase I/II open-label, dose escalation study. Int J Cancer 2022; 150:993–1006.

48. Shapiro GI, LoRusso P, Dowlati A, TD K, Jacobson CA, Vaishampayan U, et al. A phase 1 study of RO6870810, a novel bromodomain and extra-terminal protein inhibitor, in patients with NUT carcinoma, other solid tumours, or diffuse large B-cell lymphoma. Br J Cancer 2021;124:744–53.

49. Piha-Paul SA, Hann CL, French CA, Cousin S, Brana I, Cassier PA, et al. Phase 1 study of molibresib (GSK525762), a bromodomain and extra-terminal domain protein inhibitor, in NUT carcinoma and other solid tumors. JNCI Cancer Spectr 2020;4:pkz093.

50. Cheng ML, Huang Y, Luong N, LoPiccolo J, Nishino M, Sholl LM, et al. Exceptional response to bromodomain and extraterminal domain inhibitor therapy with BMS-986158 in BRD4-NUTM1 NUT carcinoma harboring a BRD4 splice site mutation. JCO Precis Oncol 2023;7:e2200633.

51. Aggarwal RR, Schweizer MT, Nanus DM, Pantuck AJ, Heath EI, Campeau E, et al. A phase Ib/IIa study of the Pan-BET inhibitor ZEN-3694 in combination with enzalutamide in patients with metastatic castration-resistant prostate cancer. Clin Cancer Res 2020;26:5338–47.

52. Aftimos PG, Oliveira M, Punie K, Boni V, Hamilton EP, Gucalp A, et al. A phase 1b/2 study of the BET inhibitor ZEN-3694 in combination with talazoparib for treatment of patients with TNBC without gBRCA1/2 mutations. J Clin Oncol 40: 16s, 2022 (suppl; abstr 1023).

53. Shorstova T, Foulkes WD, Witcher M. Achieving clinical success with BET inhibitors as anti-cancer agents. Br J Cancer 2021;124:1478–90.